JOURNAL OF NANOMATERIALS AND DEVICES
Jul - Dec 2026, VOL. 4, ISSUE 2, pp. 13-22
https://doi.org/10.61577/jnd.2026.100007

REVIEW

Cation effects and nanocomposite architectures in spinel-ferrite chemiresistive gas sensors: A critical review

Harsh Bhardwaj[1], Manisha Arya[2], Chinu Agrawal[3], Anil Kumar[4], Govind Bagaria[5], Nikita Tiwari[6], Neha Mehra[7] and Raaz K Maheshwari[8]

[1]Department of Chemistry, Shri Ratanlal Kanwarlal Patni Girls' College, Kishangarh, Ajmer, Rajasthan, India

[2]Department of Physics, Indian Institute of Science, Bengaluru, Karnataka, India

[3]Department of Physics, JCERC University, Jaipur, Rajasthan, India

[4]Department of Physics, Govt. Bangur College, Didwana-Kuchaman, Rajasthan, India

[5]Department of Physics, Mohan Lal Sukhadia University, Udaipur, Rajasthan, India

[6]Department of Physics, SBRM Govt. PG College, Nagaur, Rajasthan, India

[7]Department of Physics, Rajiv Gandhi PG College, Maulasar, Didwana-Kuchaman, Rajasthan, India

[8]Department of Chemistry, MDSU, SBRM Govt PG College, Nagaur, Rajasthan, India

ABSTRACT

NH_3, H_2S, and NO_2 detection below occupational and environmental thresholds remains constrained by poor selectivity, elevated operating temperatures, and humidity interference in single-phase ferrite chemiresistors. Spinel ferrite nanocomposites introduce two design variables absent from single-phase configurations: ferrite cation-site occupancy and composite junction architecture. This critical review covers 2015-2026 cation-engineered MFe_2O_4 nanocomposite literature across four composite architectures for NH_3, NO_2, H_2S, ethanol, acetone, and toluene.

$ZnO/ZnFe_2O_4$ hollow nanocages resolved acetone to 1 ppm at 290°C with response 25.8, outperforming both phases under matched conditions. Ni substitution produced Fe/Ni-ratio-dependent barrier sensitivity; Co substitution restricted grain growth above 200°C. Cu-bearing composites showed morphology and transport changes determined by partner phase. Ferrite/carbon composites achieved 0.02 ppm acetone at room temperature but showed unsatisfactory long-term stability. Ferrite/polymer composites enabled room-temperature NH_3 detection, operationally limited to below 150°C. Bi-ferrite heterojunctions produced no chemiresistive sensing data across any analyte in the reviewed period.

Within the reviewed period, no study links Mössbauer-confirmed A/B-site occupancy to composite junction behaviour and sensing outcome in a single experimental design. Zn/Ni co-doped ferrite nanocomposites with confirmed site occupancy and humidity-controlled testing define the primary unresolved experimental target.

KEY WORDS

Spinel ferrites; Cation engineering; Nanocomposites; Chemiresistive gas sensors; Heterojunction; Oxygen vacancies

ARTICLE HISTORY

Received 10 July 2026;
Revised 31 Jul 2026;
Accepted 10 August 2026

Introduction

NH_3, H_2S, and NO_2 define three gas monitoring thresholds at 50 ppm (OSHA PEL), 100 ppm (IDLH), and 25 µg/m^3 (WHO 24-hour guideline), with detection demand distributed across agriculture, mining, automotive emission surveillance, and clinical breath diagnostics [1-4]. Spinel ferrites are suited to this requirement because cation substitution tunes semiconducting behaviour, surface reactivity, and chemical stability across temperature ranges relevant to ionosorption-based chemiresistors [5-7]. Poor selectivity between chemically similar reducing gases, baseline drift under humid conditions, and operating temperatures above 200°C persist in single-phase ferrite sensors, and water vapour is the most consistent barrier, competing with target gas molecules at surface oxygen sites under conditions that most reported sensing data do not replicate[1,5,8]. Selectivity is further limited because NH_3 and H_2S overlap in optimal operating temperature windows and produce resistance changes in the same direction in n-type ferrites, making response magnitude alone an unreliable discrimination criterion [1,5].

Cation distribution between the 8a tetrahedral and 16d octahedral Wyckoff positions of MFe_2O_4 is the primary structural variable for ferrite gas sensing [5,9,10]. A-site substitution displaces Fe toward B sites, raising the Fe^{2+}/Fe^{3+} hopping concentration that governs polaron conduction, and B-site substitution independently introduces redox-active cation environments that alter the carrier type and shift surface adsorption site chemistry in ways that directly modulate gas-phase interaction [11-13]. DFT on cation-inverted $ZnFe_2O_4$ shifted NO_x adsorption energy from −0.1 to −0.6 eV at the oxygen-covered surface, enabling ppb-level room-temperature NO detection through site redistribution rather than particle size change [11,14]. That result separates site-specific cation engineering from generic compositional doping, which modifies ferrite properties without confirming which crystallographic positions are affected [5,15]. Cation engineering in this review denotes substitution with verified A/B-site consequence [6,11].

Single-phase ferrite sensors adjust cation composition and surface chemistry simultaneously, with no mechanism to change one without affecting the other [5,6]. Nanocomposites break this coupling [5]. Cation-determined ferrite electronic structure reaches the composite contact zone intact, where the second phase independently defines junction type and band alignment [5,16]. Ferrite-side substitution effects then propagate across the heterointerface, resetting charge transfer kinetics and depletion barrier height in a way that makes the junction a structural consequence of the cation engineering applied to

***Correspondence:** Mr. Harsh Bhardwaj, Department of Chemistry, Shri Ratanlal Kanwarlal Patni Girls' College, Kishangarh, Ajmer, Rajasthan, India. e-mail: harsh.bhardwaj0705@gmail.com

the ferrite phase [1,5,16]. That link between A/B-site occupancy and composite heterojunction behaviour is the analytical thread connecting the discussions of cation engineering and gas-sensing performance.

This review covers the 2015–2026 cation-engineered spinel ferrite nanocomposite literature across ferrite/metal oxide (Type I), ferrite/carbon nanostructure (Type II), ferrite/conducting polymer (Type III), and bi-ferrite (Type IV) configurations for six target analytes [5,6,17]. Target gases are NH_3, NO_2, H_2S, ethanol, acetone, and toluene [18-20]. Type I composites are examined because ferrite-oxide junctions establish n-n, p-n, or p-p configurations depending on ferrite carrier type, modifying depletion layer physics and lowering optimal sensing temperature relative to single-phase ferrites [16]. Type II composites enter because carbon networks alter interfacial charge transport and produced the lowest detection limits in the reviewed ferrite composite dataset [21]. Polymer-ferrite composites address room-temperature NH_3 sensing, and biferrite composites address internal junction behaviour between complementary ferrite phases [22,23]. Single-phase ferrites, magnetic studies, photocatalytic and biomedical applications are excluded [6,15,24]. Coverage across analytes reflects the actual distribution of composite ferrite chemiresistive publications: acetone and VOC sensing dominate the available dataset while NO_2, H_2S, and toluene remain underrepresented in composite-specific studies.

Literature for this review was identified through Google Scholar, Web of Science, and Scopus using search terms including spinel ferrite, MFe_2O_4, nanocomposite, chemiresistive, gas sensor, cation substitution, and heterojunction, restricted to 2015-2026. Studies reporting composite ferrite chemiresistive sensing performance or structural characterisation directly relevant to composite gas-sensing behaviour were included. Single-phase ferrite studies, magnetic property studies, and composite ferrites developed for photocatalytic, biomedical, or microwave absorption applications were excluded.

Spinel Ferrites: Crystal Structure, Sensing Fundamentals and Composite Classification

Crystal structure and cation site configuration

MFe_2O_4 spinel ferrites crystallize in space group Fd3m on a cubic close-packed oxygen sublattice that defines two distinct cation environments: tetrahedral A sites (8a Wyckoff) and octahedral B sites (16d Wyckoff) [5,9,10]. The unit cell contains 8 A and 16 B positions [10,25] These counts arise from one-eighth of all tetrahedral voids and one-half of all octahedral voids being occupied, and lattice parameters across representative MFe_2O_4 compositions span 8.3–8.5 Å, with values near 8.34 Å and 8.37–8.39 Å documented for distinct stoichiometries (Figure 1) [10,25,26].

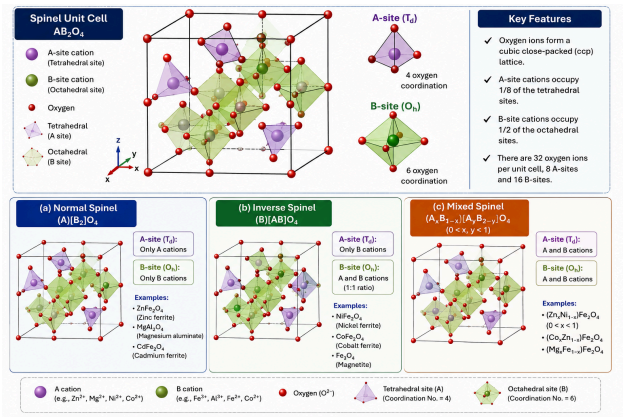

Figure 1. Spinel unit cell with A and B sites labeled; normal vs inverse vs mixed configurations with named examples. Original schematic only, not redrawn from a single source.

Whether M^{2+} and Fe^{3+} distribute as normal, inverse, or mixed spinels depends on the site-energy preference of the divalent cation [25,26,28]. $ZnFe_2O_4$ is the canonical normal spinel, with Zn^{2+} at A sites and Fe^{3+} at B sites [10,26,28]. $NiFe_2O_4$ and $CoFe_2O_4$ are inverse spinels in which Fe^{3+} occupies A sites while M^{2+} and Fe^{3+} share B sites, and compositions between the two extremes are described by an inversion parameter λ recording the fraction of M^{2+} displaced to octahedral coordination [9,10,25]. Site occupancy governs which cations are exposed at grain surfaces and composite interfaces, directly determining the adsorption and charge-transfer pathways available for gas sensing [9,28].

Electrical conduction and gas sensing mechanism

Small polaron hopping governs electrical transport in polycrystalline spinel ferrites [12,13,29]. Electron transfer between Fe^{2+} and Fe^{3+} on octahedral B sites provides the primary conduction pathway, with hopping site density and accessibility modulated by mixed-valence cation occupancy and site distribution [28,29]. Grain-boundary resistance, not bulk grain conductivity, dominates the net chemiresistive output in most polycrystalline ferrite sensors [12,13,26]. Carrier type divides the ferrite family under standard synthesis conditions: $NiFe_2O_4$ and $CoFe_2O_4$ are commonly reported as p-type while $ZnFe_2O_4$ is typically n-type, though all three shift with defect state, stoichiometry, and annealing atmosphere, and this distinction determines which junction class forms when a ferrite couples with a composite second phase [5,16,25,30,31].

Chemiresistive response depends on sequential oxygen ionosorption at the oxide surface [5,30,32]. Below approximately 150°C, adsorbed O_2 captures surface electrons to form O_2^-; between 150 and 300°C, activation proceeds as $O_2^- + e^- \rightarrow 2O^-$, raising surface acceptor density [30,33]. Oxygen vacancies replenish these acceptor sites [30,33,34]. In n-type ferrites, reducing gas exposure returns electrons to the conduction band, decreasing resistance; Ra/Rg applies to reducing gases and Rg/Ra to oxidizing gases for n-type systems. Both directions reverse in p-type ferrites, where reducing gases deplete hole carriers and raise resistance while oxidising gases lower it [5,30,32]. CuS formation on Cu-containing sensing phases during H_2S exposure represents a chemical transformation mechanism that supplements ionosorption and is examined in the discussion of cation engineering and composite architecture [34].

Composite classification

Four composite architectures organise the gas-sensor literature covered in this review [5]. Type I (Ferrite/Metal Oxide) pairs a ferrite with ZnO, SnO_2, TiO_2, In_2O_3, or WO_3, and the oxide-oxide contact generates a heterojunction that modifies depletion layer width and barrier height depending on the carrier types of both components [5,16]. Type II (Ferrite/Carbon Nanostructure) uses rGO, graphene, MXenes, or CNTs with Schottky-like or ohmic contact character set by work function alignment between the ferrite and the carbon component [21]. Type III couples ferrites with PANI or PPy to enable room-temperature response, with the practical ceiling imposed by polymer thermal degradation above approximately 150°C [27]. Type IV (Bi-Ferrite) pairs two spinel ferrites of complementary carrier type to form an internal p-n junction, and their shared crystal structure reduces interfacial structural discontinuity relative to ferrite-oxide pairings [5,30]. This taxonomy structures the following discussion [5].

Synthesis of Spinel Ferrite Nanocomposites

The synthesis route determines ferrite particle size, crystallinity, and interfacial contact quality with the composite second phase, three structural variables that directly condition sensing performance.

Co-precipitation

Aqueous metal salt solutions are brought to controlled pH by dropwise addition of NaOH or NH_4OH under mechanical agitation and mild heating at 80–100°C, precipitating metal hydroxides that convert to the ferrite phase on continued thermal treatment [36]. Particle sizes in co-precipitated ferrites typically fall within 10–30 nm, with

https://doi.org/10.61577/jnd.2026.100007

distributions narrowing when surfactants or controlled reagent addition rates are employed [36,37]. The second phase is introduced into the precipitation medium before ferrite nucleation, so growing ferrite nuclei form on or around a pre-existing substrate, a geometry well-suited to Type II composites built on carbonaceous supports such as rGO. Post-synthesis annealing improves crystallinity but drives grain growth and reduces effective contact area at the ferrite-second phase boundary, which is the primary structural cost of this route. $CoFe_2O_4$/ZnS composites produced this way demonstrate that both phases integrate during precipitation without separate high-temperature processing steps [36].

Sol-Gel auto-combustion

Stoichiometric metal nitrates and a chelating organic fuel (citric acid, gelatin, or polyacrylic acid) dissolved in aqueous solution form a viscous gel that undergoes self-sustaining ignition, yielding phase-pure ferrite in a single thermal step. Combustion intensity, cation homogeneity, and ferrite crystallinity all respond to the fuel-to-nitrate ratio, and product particle sizes before further annealing fall in the 20–50 nm range. Precursors for the composite second phase are dissolved or dispersed into the sol before gelation, producing intimate ferrite-oxide contact after combustion and making this route well-suited to Type I composites [36]. Carbon-based second phases (rGO, CNTs) oxidize during the self-sustaining thermal reaction, rendering this route incompatible with Type II composites [36,38]. $CoFe_2O_4$-SiO_2 composites produced by incorporating silica precursors into the gel before ignition illustrate the route's capacity for generating interpenetrating oxide-oxide networks (Figure 2) [36].

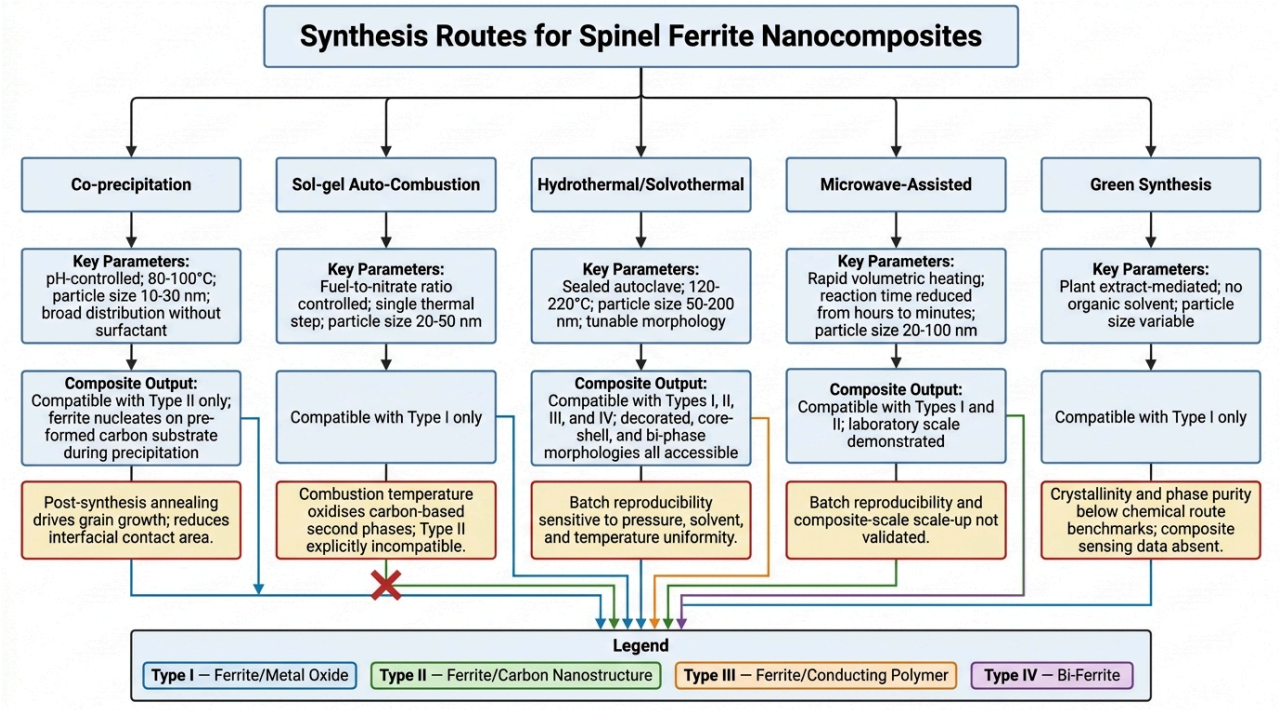

Figure 2. Synthesis routes for spinel ferrite nanocomposites showing particle size range, compatible composite architecture types (I-IV), and primary limitation for composite formation. Particle size ranges represent as-synthesized ferrite phase dimensions. Crossed symbol indicates route incompatibility with the specified composite type.

Hydrothermal, microwave, and green synthesis

Sealed autoclave conditions at 120–220°C give hydrothermal and solvothermal processing simultaneous control over ferrite nucleation rate, crystal morphology, and second-phase integration geometry, with less agglomeration than low-temperature wet routes. Second-phase incorporation follows two distinct strategies: growing ferrite directly on a pre-formed substrate (rGO sheet or oxide support) yields decorated morphologies with high interfacial contact area, while co-processing both phases within the same autoclave step produces core-shell or bi-phase architectures, with both strategies documented across all four composite types. Reproducibility depends on autoclave pressure, solvent identity, surfactant concentration, and temperature uniformity, complicating transfer between laboratory and production scale [36].

Reaction times shrink from hours to minutes under microwave dielectric heating, with resulting crystallinity matching hydrothermal benchmarks in laboratory-scale demonstrations, but composite batch reproducibility has not been validated at scale [36]. Plant extracts replace organic solvents in green synthesis, functioning simultaneously as reducing, capping, and stabilising agents and

enabling Type I composite formation at lower temperatures, but ferrite crystallinity and phase purity in these products are more variable than in combustion or hydrothermal routes, and composite-specific sensing data for both emerging methods remain too sparse to benchmark them against established approaches (Table 1) [36,38].

https://doi.org/10.61577/jnd.2026.100007

Table 1. Synthesis routes for spinel ferrite nanocomposites: Particle size, composite morphology, compatible types, and primary limitation.

Method	Size (nm)	Compatible types	Primary limitation	References
Co-precipitation	10–30	Type II	Annealing improves crystallinity but drives grain growth and reduces interfacial contact	[36,37]
Sol-gel auto-combustion	20–50	Type I	Combustion temperature oxidises carbon-based second phases; Type II incompatible	[36]
Hydrothermal/solvothermal	50–200	Types I–IV	Morphology reproducibility sensitive to pressure, solvent, and temperature uniformity	[36,39]
Microwave-assisted	20–100	Types I–II	Batch reproducibility and composite-scale scale-up not demonstrated	[36,38]
Green synthesis	Variable	Type I	Phase purity and crystallinity below chemical route benchmarks; composite sensing data absent	[36,38]

Cation Engineering and Composite Architecture in Ferrite Gas Sensors

Cation site effects on ferrite electronic structure

Five parameters structure the analysis of cation substitution in ferrite nanocomposites: site occupancy at A or B positions, lattice parameter shift, oxygen-vacancy generation, conductivity change, and composite sensing outcome [5,6]. Mössbauer spectroscopy, XAS/EXAFS, and neutron diffraction resolve cation oxidation states, partial site occupancies, and inversion profiles in the ferrite phase, while impedance spectroscopy characterizes grain and grain-boundary resistance contributions independently [9,12,13]. In a composite, those ferrite-side parameters carry into heterojunction behavior because ferrite carrier type, vacancy chemistry, and surface reactivity collectively set the interfacial barrier height, depletion width, and charge-transfer rate to the partner material [5,16,40]. Two constraints apply specifically to composites and carry through each dopant subsection: configuration can invert ferrite carrier type independently of composition, shown by n-type and p-type responses from identically composed $Mg_{0.5}Zn_{0.5}Fe_2O_4$ nanotubes under different geometric embedding conditions, and carrier type for specific ferrite phases varies across the literature with synthesis and defect state rather than being fixed by stoichiometry alone [5,16,31].

Zn-substituted ferrites

$ZnFe_2O_4$ is among the most studied ferrite phases for chemiresistive sensing, with element doping and heterostructure formation identified as its principal performance routes [5,7]. Band-gap offset at the ZnO-$ZnFe_2O_4$ contact drives a temperature-dependent n-p-n conductive switch in hollow ZnO/$ZnFe_2O_4$ microspheres during VOC sensing, as carrier partitioning between the two phases shifts with temperature and reducing-gas electron injection. Hollow nanocage ZnO/$ZnFe_2O_4$ architecture reached response 25.8 to 100 ppm acetone at 290 °C with a 1 ppm detection limit, exceeding both ZnO hollow nanocages and $ZnFe_2O_4$ nanospheres tested under identical conditions. Adding Au decoration to produce ternary ZnO/$ZnFe_2O_4$/Au porous nanonets raised the response to 30.3 with 1 s response time and 59 s recovery, roughly three times the undecorated binary value. The interface origin of this performance cascade is documented in the reviewed literature; the site-level cation mechanism within the ferrite lattice is not directly resolved [5].

Ni-substituted ferrites

The carrier type for $NiFe_2O_4$ is not consistent across the reviewed literature: one ferrite materials review assigns it n-type character while a gas-sensor heterojunction review places p-$NiFe_2O_4$ as a component in a p-p composite with NiO, pointing to synthesis conditions and defect equilibrium as the governing variables rather than composition alone [16,31]. Composite performance data are more internally consistent. Optimal Fe/Ni ratio in NiO nanosheets bearing in situ formed $NiFe_2O_4$ nanoparticles produced a response of approximately 23 to 50 ppm acetone at 280°C, attributed to barrier height reduction at the heterojunction surface under gas exposure, and NiO/Ni-ferrite composites altered analyte selectivity relative to pure Ni-ferrite, confirming that the interface modifies sensing chemistry rather than just amplifying response [16,41]. Reliable junction-class assignment for $NiFe_2O_4$-based composites requires synthesis-controlled carrier characterisation before p-n or p-p designation can be made [16,31].

Co-substituted ferrites

Co-substituted ferrites carry stronger evidence for microstructural stability than for uniquely advantaged interfacial sensing chemistry [42,43]. A cobalt ferrite nanocomposite on an interdigitated electrode structure demonstrated ethanol sensitivity, dynamic range, and selectivity at concentrations down to 7 ppm [42]. Direct evidence for Co A/B site redistribution, lattice contraction, or non-monotonic resistivity in gas-sensing composite systems is absent from the reviewed literature [42,43]. Preserving interfacial contact area and structural integrity at elevated operating temperatures is the best-documented composite role for Co substitution, making synthesis route selection for morphology control a more productive lever than Co compositional variation at the current state of composite gas-sensing evidence [39,43].

Cu-substituted ferrites

Cu incorporation modifies composite morphology distinctively: replacing Ni^{2+} with Cu^{2+} in $Co_{0.5}Zn_{0.25}M_{0.25}Fe_2O_4$ coupled to TiO_2 changed nanocomposite morphology relative to the Ni-substituted analog [45]. PANi-$CoFe_2O_4$ nanocomposite films demonstrated trace-level NH_3 sensing at room temperature with response exceeding single-phase $CoFe_2O_4$, confirming that the polymer-ferrite junction adds a detection pathway absent in the single-component material [23]. The Jahn-Teller-to-vacancy mechanism and CuS formation during H_2S sensing are not directly established in the reviewed literature, though the documented sensitivity of Cu-bearing ferrite composites to partner phase and architecture makes this class a high-priority target for interface-resolved studies [31,41].

Rare-earth-substituted ferrites

La-substituted Co-Zn ferrite showed improved NH_3 sensitivity and

https://doi.org/10.61577/jnd.2026.100007

surface area relative to undoped Co-Zn ferrite, and Ce-substituted $MgFe_2O_4$ reached improved acetone response compared to undoped $MgFe_2O_4$. Tb-doped Fe_2O_3 nanotubes reached a response of 53.2 to 50 ppm acetone at 170 °C, attributed in part to elevated oxygen vacancy concentration from the large aliovalent substituent [20,45]. Systematic data on RE site occupancy thresholds, secondary phase formation, or ferrite-second phase contact zone chemistry in RE-doped composite systems are absent from the reviewed literature [6,40,45]. Direct characterisation at the ferrite-partner contact zone is the clearest experimental gap for the RE dopant class because RE segregation is predicted at exactly the location where composite sensing performance is determined but has not been measured in a gas-sensing context [6,31].

Composite architecture and interfacial design

The carrier type determined by cation engineering in the discussion of cation site effects defines the junction character of the composite. Four architectures produce distinct interfacial barriers: Type I (ferrite/metal oxide) generates oxide-oxide heterojunctions, Type II (ferrite/carbon nanostructure) generates Schottky or ohmic contacts, Type III (ferrite/conducting polymer) generates organic-inorganic junctions, and Type IV (bi-ferrite) generates internal junctions between complementary ferrite phases [5,16]. Response amplification in all four cases originates at the interface rather than from either component individually. Band alignment at the contact governs whether the depletion layer widens or narrows during gas exposure, with direction set by the relative electron affinity and work function of both phases [16,40].

Type I oxide-oxide junctions span n-n, p-n, and p-p configurations depending on the carrier types of both the ferrite component and the oxide partner selected [5,16]. Each configuration differs in depletion layer width and interfacial potential barrier height [16]. In n-n systems ($ZnFe_2O_4$/ZnO, $ZnFe_2O_4$/SnO_2), depletion extends from the lower-electron-affinity phase; p-n junctions such as $NiFe_2O_4$/ZnO project a built-in field into both phases, raising baseline resistance and amplifying response; p-p composites such as $NiFe_2O_4$/NiO replace depletion-layer physics with carrier balance between phases as the dominant modulation mechanism [16,40]. $NiFe_2O_4$/NiO nanosheets achieved approximately 23 responses to 50 ppm acetone at 280 °C through Fe/Ni-ratio-controlled barrier adjustment at the p-p junction [16]. The ZnO/$ZnFe_2O_4$ n-n case is documented in the discussion of cation site effects [5]. Band alignment from cation engineering determines which phase donates electrons during gas exposure; junction type, therefore, cannot be designed independently of the dopant choices in the preceding discussion [16,40].

Type IV (bi-ferrite) composites form internal p-n junctions from two spinel ferrites of complementary carrier type, with shared crystal structure reducing lattice mismatch relative to ferrite-oxide pairings. Systematic comparative data for Type IV systems in ferrite gas sensing are absent from the reviewed literature, and junction dynamics at the ferrite-ferrite contact zone remain unresolved [5].

Type II (ferrite/carbon nanostructure) composites use rGO, graphene, MXenes, or CNTs as the second phase, with Schottky-like or ohmic contact determined by work-function alignment between the ferrite and the carbon component. rGO/metal oxide composites consistently improve sensing over single-phase oxides by increasing accessible surface area and modifying interfacial charge carrier mobility. Ferrite/graphene systems show improved carrier transport through the graphene network, with rGO/metal oxide composites consistently enhancing accessible surface area and interfacial charge carrier mobility relative to single-phase ferrites [21].

Type III (ferrite/conducting polymer) composites pair ferrites with PANI or PPy to establish room-temperature chemiresistive sensing through polymer-oxide junctions [22,42]. Flexible PANi-$CoFe_2O_4$ nanocomposite films demonstrated trace-level NH_3 sensing at room temperature, with the polymer-ferrite junction amplifying response beyond single-phase values [23]. Polymer thermal degradation above approximately 150 °C sets the operational ceiling for all Type III architectures [41,42].

Morphological architecture within each composite class independently conditions sensing outcomes. One-dimensional electrospun structures deliver high surface-area-to-volume ratios and controlled pore channels that improve gas diffusion to the active ferrite-second phase contact [43]. Decorated morphologies, with ferrite nanoparticles on a second-phase substrate, maximize interfacial contact area; core-shell architectures require gas diffusion through the outer shell before reaching the junction, reducing response at equivalent composition; mixed-phase configurations occupy an intermediate position [5,43]. Ferrite-composite literature identifies morphology control and ion substitution as complementary rather than independent performance levers, and systematic mechanistic studies relating weight ratio to depletion width or vacancy accessibility are absent from the composite gas-sensing corpus [5,47].

Interface coupling and research gap

Three propositions are consistently supported across the reviewed literature regardless of composite type or dopant class. Cation distribution between A and B sites is a primary electronic control variable in spinel ferrites; substitution modifies surface chemistry and electronic structure in ways that alter gas adsorption, and heterojunction construction amplifies sensing through interfacial barrier modulation [5,6,16]. The absent step connects them: no study in the reviewed literature systematically links verified cation site occupancy in the ferrite phase to composite junction type, barrier height, and sensing output through a single controlled experimental design [5,6].

That link matters because composite architecture can override single-phase ferrite predictions, as the $Mg_{0.5}Zn_{0.5}Fe_2O_4$ embedding experiment demonstrates: configuration alone inverts carrier type without any compositional change [5]. The gap is sharpest for co-doping. Zn^{2+} redistributes Fe to B sites, raising the hopping carrier pool, while Ni^{2+} at B sites introduces a second redox-active cation environment. Whether these effects are additive in composite form has not been tested in any study in the reviewed literature. Cu + Zn carries similar logic through two independent vacancy generation mechanisms. No composite study with confirmed co-dopant site occupancy, systematic ratio variation, and humidity-resolved sensing data exists for either combination [5,6]. Ferrite and sensor literature repeatedly identifies deliberate interface characterisation and structure-property resolution as primary unmet needs [6,31].

Composite architecture can override single-phase ferrite carrier type predictions without any compositional change, demonstrated by n-type and p-type responses from identically composed $Mg_{0.5}Zn_{0.5}Fe_2O_4$ nanotubes under different geometric configurations [9]. Four evidence gaps follow directly from the reviewed dataset. No study combines Mössbauer-confirmed A/B-site occupancy with systematic dopant ratio variation and humidity-controlled sensing for any single cation class in a composite gas-sensing architecture [5,6]. Cu-substituted composite H_2S cycling data beyond seven days are absent from all reviewed studies [5,41]. RE dopant effects at the ferrite-second phase contact zone remain structurally uncharacterised, despite RE segregation concentrating at that interface [6,40]. No single cation-engineered ferrite composition has been tested across all four composite types under matched experimental conditions (Table 2) [5,6].

https://doi.org/10.61577/jnd.2026.100007

Table 2. Cation substitution effects on ferrite electronic structure, expected composite junction, and confirmation status in indexed composite gas sensing.

Dopant	Preferred site	Vacancy generation	Conductivity change	Composite evidence	Grade	Reference
Zn^{2+}	A (tetrahedral)	Indirect; Fe^{3+} redistribution to B sites	Lowered resistivity; n-type strengthened	$ZnO/ZnFe_2O_4$ nanocages: response 25.8 to 100 ppm acetone at 290°C; 1 ppm LOD	C	[5,9,10,7]
Ni^{2+}	B (octahedral)	Moderate via Ni^{2+}/Ni^{3+} redox couple	Carrier-type synthesis-dependent; dual redox couple active	$NiFe_2O_4/NiO$: response ~23 to 50 ppm acetone at 280°C; selectivity altered vs pure Ni-ferrite	C	[16,25,31]
Co^{2+}	Mixed A and B	Moderate; site redistribution-dependent	Non-monotonic resistivity with substitution level	Cobalt ferrite composite: ethanol to 7 ppm; no A/B-site confirmation in indexed composite study	S	[14,25,47]
Cu^{2+}	B (octahedral); Jahn-Teller active	High; direct structural consequence of CuO_6 elongation	Cu^{+}/Cu^{2+} redox couple; conductivity raised in CNT composite	PANI/Cu-ferrite: NH_3 response exceeded pure Cu-ferrite at RT; CuS mechanism unverified in composite	S	[23,45]
RE^{3+}	Grain boundary above x ≈ 0.05	High at boundaries; $REFeO_3$ above x ≈ 0.10	Grain growth pinned; bulk conductivity unaffected	Ce and La doping improved sensitivity in single-phase; contact zone uncharacterised in composites	S	[20,40,43,45]
Zn^{2+} + Ni^{2+}	A (Zn) + B (Ni)	Moderate to high; additive mechanisms	Combined n-type strengthening and dual redox activity	No indexed composite study with confirmed occupancy and humidity-controlled data	H	[5,6]

C = Confirmed in indexed composite gas-sensing study

S = Established in single-phase ferrite literature; composite-specific confirmation absent

H = Hypothesis, neither single-phase nor composite confirmation available

Comparative Gas Sensing Performance

Composite ferrite sensing data in the reviewed literature concentrate on acetone and VOC detection. Organising performance by composite architecture type rather than by analyte reflects actual coverage and avoids implying balanced gas-target data where none exists.

Type I: Ferrite/metal oxide composites

$ZnO/ZnFe_2O_4$ hollow nanocages registered response 25.8 to 100 ppm acetone at 290°C and resolved the analyte to 1 ppm. ZnO hollow nanocages and $ZnFe_2O_4$ nanospheres tested independently under identical conditions both underperformed the composite, which localises the gain at the oxide-oxide contact rather than in either phase. Au-functionalised $ZnO/ZnFe_2O_4$ porous nanonets extended response to 30.3 with 1 s response time and 59 s recovery, approximately three times the undecorated binary values [5]. A second $ZnO/ZnFe_2O_4$ morphology covered 5 to 700 ppm acetone at 250°C [48]. In a p-p type I architecture, $NiFe_2O_4$-decorated NiO nanosheets at Fe/Ni-24.9 composition reached a response of approximately 23 to 50 ppm acetone at 280°C, with the performance optimum tracking the compositional ratio rather than total ferrite loading [16]. NH_3, NO_2, and H_2S data are absent for all Type I ferrite composites in the reviewed literature.

Type II: Ferrite/carbon nanostructure composites

$rGO/WO_3/ZnFe_2O_4$ reached response 26.92 to acetone with a 0.02 ppm detection limit and 51 s response time, exceeding both WO_3 and $ZnFe_2O_4$ individually under matched conditions. $ZnFe_2O_4$/graphene quantum dot composites operated at room temperature and covered acetone from 5 ppm at a response of 1.2 to 1000 ppm at a response of 13.3, with response and recovery times each under 12 s; long-term stability was reported as unsatisfactory in the same study [5]. Room-temperature operation in these two Type II systems distinguishes the carbon composite architecture from Type I entries, which required 250–290°C to reach comparable response values [5,48]. NH_3, H_2S, and toluene data for ferrite/carbon composites are absent from the reviewed literature.

Type III: Ferrite/conducting polymer composites

PANI/Cu-ferrite films produced higher NH_3 response at room temperature than Cu-ferrite alone under matched conditions, with the polymer-ferrite junction contributing a charge transfer pathway inactive in the single-component material [41]. SnO_2/PANI, a non-ferrite reference case spans 10 ppb to 100 ppm NH_3 at room temperature, a concentration window against which no ferrite-polymer composite has yet been benchmarked [48]. Thermal degradation of the conducting polymer above approximately 150°C limits all Type III architectures, and no indexed ferrite-polymer composite study reports stability data beyond 7 days of continuous operation [26,42].

Type IV: Bi-ferrite composites

Table 3. Indexed composite spinel ferrite gas sensing performance (2015-2026) organised by composite type.

Type	Material	Gas	Temp (°C)	Response	LOD	Response/Recovery (s)	Humidity	Stability	Ref
I	$ZnO/ZnFe_2O_4$ hollow nanocages	Acetone	290	25.8 (100 ppm)	1 ppm	—	—	—	[5]
I	$ZnO/ZnFe_2O_4$/Au nanonets	VOC	—	30.3	—	1/59	—	—	[5]
I	$ZnO/ZnFe_2O_4$	Acetone	250	—	5 ppm	—	—	—	[48]

https://doi.org/10.61577/jnd.2026.100007

Table 3 (continued)

Type	Material	Gas	Temp (°C)	Response	LOD	Response/Recovery (s)	Humidity	Stability	Ref
I	$NiFe_2O_4$/NiO nanosheets	Acetone	280	~23 (50 ppm)	—	—	—	—	[16]
II	rGO/WO_3/$ZnFe_2O_4$	Acetone	—	26.92	0.02 ppm	51/—	—	—	[5]
II	$ZnFe_2O_4$/graphene QD	Acetone	RT	1.2-13.3 (5-1000 ppm)	5 ppm	<12/<12	—	Unsatisfactory	[5]
III	PANI/$CoFe_2O_4$	NH_3	RT	Above single-phase	—	—	—	—	[23]

Bi-ferrite Type IV composites carry no performance entries in the indexed gas sensing literature. Whether a ferrite-ferrite p-n junction produces a response distinct from single-phase ferrite behaviour under gas exposure has not been tested for any analyte or operating condition. A direct comparison between $NiFe_2O_4$/$ZnFe_2O_4$ and each isolated constituent would close this gap at the minimum experimental cost [5].

Response reported as Ra/Rg for reducing gases on n-type systems and Rg/Ra for oxidising gases with direction reversing for p-type systems. Dashes indicate data unreported in the cited study. Type IV bi-ferrite composites produced no chemiresistive sensing data for any analyte in the reviewed period.

Challenges and Future Perspectives

Selectivity

Cross-sensitivity between NH_3 and H_2S is structurally difficult to resolve in ferrite composite systems because both gases reduce surface-adsorbed oxygen species through electron donation, generating resistance changes in the same direction and at comparable magnitude in n-type architectures [1,5]. Selectivity stands as a primary barrier to chemiresistive sensor commercialisation across metal oxide platforms, and ferrite composites have not addressed this at the junction level [1]. Temperature-selective windows, in which different analytes produce maximum response at different operating temperatures, have been described as a partial strategy in single-phase oxide systems but remain unvalidated for any ferrite composite architecture in the reviewed literature [1,48]. No study in the reviewed literature demonstrates analyte discrimination in a ferrite composite through deliberate heterojunction design, meaning through controlled variation of junction type or barrier height rather than through empirical observation of differential response ratios between gases [5,16]. Pattern recognition on arrays of differently cation-engineered ferrite composites offers a near-term path to discrimination that does not require fundamental advances in single-sensor sensing chemistry, but this approach has not been implemented for any ferrite composite configuration in the reviewed literature [1,5].

Humidity interference

Most chemiresistive sensing studies, including composite ferrite work, are conducted below 40% relative humidity, a condition that does not replicate agricultural environments, mining atmospheres, or clinical exhaled-breath matrices where NH_3 and H_2S monitoring is targeted [1,2,8]. Water vapor competes with analyte molecules at surface oxygen adsorption sites, reducing accessible vacancy density and shifting baseline resistance in ways that fixed-temperature calibration cannot reliably correct [2,8]. For ferrite composites specifically, whether p-n depletion barriers widen or narrow as water vapor displaces adsorbed oxygen at the heterojunction has not been examined for any composite type in the reviewed literature [5,16,43]. This is not a minor calibration issue: humidity shifts that alter the baseline depletion state modify both the magnitude and apparent direction of response to a fixed analyte concentration, not only the signal-to-noise ratio [1,5]. Temperature-modulated humidity compensation, discussed in the broader oxide sensor literature, remains experimentally unvalidated for ferrite composite architectures of any type [1]. Type III polymer-ferrite composites carry an additional vulnerability because conducting polymer networks are more permeable to water vapor than oxide-oxide contacts at equivalent temperatures, undermining the practical value of room-temperature operation [23,41].

Long-term stability

The only direct long-term stability observation in the reviewed composite ferrite corpus is the unsatisfactory durability reported for $ZnFe_2O_4$/graphene quantum dot composites during acetone cycling; no other entry in Table 3 addresses the question at all [5]. Extended performance records beyond 7 days of continuous operation are absent for every other composite ferrite architecture in this review, which means published response values and detection limits are single-session measurements without a validated durability basis. For Cu-substituted composite systems, the CuS reversibility question is separately unresolved. Cu^{2+} can react with H_2S to form conductive CuS, adding a chemical transformation response pathway alongside ionosorption, but whether CuS reconverts during recovery and whether composite architecture modifies this conversion kinetics has not been tested in any study in the reviewed literature [5,41]. Distinguishing drift from heterojunction barrier degradation versus ferrite phase structural change as the primary failure mechanism requires operando characterisation techniques not yet applied to any ferrite composite gas sensor [6,15].

Operating temperature and architecture conflict

Type I composite entries in Table 3 produced their strongest response values at 250–290°C. Type II composites operated at room temperature in the reviewed dataset, with rGO/WO_3/$ZnFe_2O_4$ achieving 0.02 ppm acetone and $ZnFe_2O_4$/graphene QD covering 5–1000 ppm acetone at room temperature, though the latter reported unsatisfactory long-term stability [5]. Type III polymer-ferrite composites operate at room temperature but lose structural integrity above approximately 150°C, making the two architecture classes mutually exclusive across a temperature range that represents a substantial gap in the design space [23,41]. Room-temperature operation without a polymer phase is achievable within Type II, as the $ZnFe_2O_4$/graphene quantum dot and rGO/WO_3/$ZnFe_2O_4$ entries demonstrate, but the reported instability of the quantum dot system shows that room-temperature Type II performance currently trades durability for reduced thermal requirement [5]. MXene-ferrite composites are the most frequently cited candidate for bridging this gap, with a preliminary room-temperature response documented in recent studies, but the sensing mechanism at the ferrite-MXene contact is uncharacterised, and operating condition control is insufficient to permit direct comparison with Type I benchmarks [14,43].

https://doi.org/10.61577/jnd.2026.100007

Future priorities

Four experimental targets follow from the gaps documented throughout the discussion of cation engineering and gas-sensing performance, ordered by clarity of the mechanistic basis supporting each.

Zn/Ni co-doped ferrite nanocomposites carry the strongest mechanistic basis of the four gaps identified in the discussion of interface coupling and research gaps. Zn^{2+} A-site preference forces Fe^{3+} toward B sites, raising the hopping carrier pool, while Ni^{2+} at B sites introduces a second redox-active cation environment through the Ni^{2+}/Ni^{3+} couple; the two effects are mechanistically additive and independently grounded in established single-phase ferrite data [5,6]. No composite study has combined Mössbauer-confirmed occupancy with systematic Zn:Ni ratio variation and humidity-controlled testing in a single experimental design [5,6,11].

Cu-substituted composite H_2S stability requires targeted cycling experiments. CuS formation is proposed as a chemical transformation pathway alongside ionosorption, but whether this conversion occurs and reverses under composite conditions across repeated exposure cycles has not been measured in any study in the reviewed literature [5]. Without that data, single-session response values cannot justify deployment.

RE dopant characterisation at the ferrite-second phase contact zone is the lowest-cost experiment relative to its return. RE ions are predicted to concentrate above $x \approx 0.05$ at grain boundaries and ferrite-partner contact zones based on ionic size exclusion from A and B sites, but direct structural confirmation at composite interfaces is absent from the reviewed literature [6,40]. Mössbauer spectroscopy or high-resolution TEM applied specifically to this interface region in a gas-sensing composite would resolve whether RE boundary effects differ from bulk grain-boundary pinning.

Systematic testing of one cation-engineered ferrite composition across all four composite types under matched conditions does not exist, which means cation effects and architecture effects remain entangled throughout the reviewed dataset [5,6].

Limitations

Acetone and VOC studies dominate the reviewed dataset while NO_2, H_2S, and toluene coverage in composite ferrite chemiresistors remains thin. Toluene is absent from the performance record entirely. Most reviewed studies vary ferrite composition and composite architecture simultaneously, so cation effects and junction effects cannot be separated from the available data. Published response values reflect dry single-session test conditions because stability and humidity-resolved measurements are unreported across almost all entries. Carrier type assignments for $NiFe_2O_4$ and $CoFe_2O_4$ vary between sources and depend on synthesis-specific defect states that are rarely characterised in gas-sensing studies.

Conclusions

Cation engineering of the ferrite phase controls carrier density, oxygen vacancy generation, and surface electronic structure, and in nanocomposites those properties propagate to the ferrite-second phase junction to govern depletion layer behaviour and analyte response. $ZnO/ZnFe_2O_4$ composites are the clearest documented case, with interfacial response gains over each isolated phase confirming the oxide-oxide junction as the active performance element. Ni substitution produced the most barrier-sensitive junction behaviour across the dopant classes reviewed. Co-substitution contributed microstructural stability at elevated operating temperatures rather than uniquely advantaged sensing chemistry. Cu substitution altered composite morphology and carrier transport in partner-phase-dependent ways, and the H_2S chemical transformation mechanism attributed to Cu sites remains unconfirmed in any composite cycling study.

Type I composites produced the highest absolute response values at elevated temperatures. Type II carbon composites achieved the lowest detection limits alongside partial room-temperature operation, though long-term stability was flagged as unsatisfactory in the only study in the reviewed literature that examined it. Type III polymer composites enabled room-temperature sensing but cannot sustain structural integrity above 150°C. Type IV bi-ferrite composites produced no gas-sensing data in any study in the reviewed literature.

Selectivity between reducing gases remains unresolved across all four composite types. Humidity-resolved performance data and stability records extending beyond one week are absent from the reviewed literature for every analyte and composite architecture reviewed, which means published detection limits and response values describe dry, short-duration conditions only.

Cation site occupancy and composite junction type are independently documented as performance variables throughout this review. Their combination within a single dopant-resolved composite experiment has not been demonstrated for any of the five dopant classes covered here. Zn/Ni co-doped ferrite nanocomposites with Mössbauer-confirmed site occupancy and humidity-controlled sensing are the primary experimental target because they directly test whether ferrite-side cation engineering propagates to composite junction behavior. Cu-substituted composites under repeated H_2S cycling would answer whether CuS formation reverses in composite form, a question single-session response data cannot resolve.

Data Availability Statement

This manuscript is a review article. No new experimental data were generated or analysed during this study. All data discussed are available in the published references cited within the manuscript.

Funding Statement

This research received no external funding.

Conflict of Interest Statement

The authors declare no conflicts of interest.

Author Contributions Statement

Harsh Bhardwaj: Conceptualisation, writing (original draft), writing (review and editing), project administration, and corresponding author.

Manisha Arya: literature collection, writing (review and editing). Chinu Agarwal: literature collection, writing (review and editing).

Anil Kumar: Writing (review and editing), supervision. Govind Bagaria: literature collection, writing (review and editing).

Nikita Tiwari: Literature collection.

Raaz K. Maheshwari: Writing (review and editing), supervision. All authors have read and approved the final version of the manuscript.

Ethics Declaration

This article is a review of previously published literature. It does not involve human participants, animal subjects, clinical data, or any material requiring institutional ethics approval. No ethics committee clearance was required for this work.

Reference

1. Bulemo PM, Kim DH, Shin H, Cho HJ, Koo WT, Choi SJ, et al. Selectivity in chemiresistive gas sensors: Strategies and challenges. Chem Rev. 2025;125(8):4111-4183. https://doi.org/10.1021/acs.chemrev.4c00592
2. Li HY, Lee CS, Kim DH, Lee JH. Flexible room-temperature NH_3 sensor for ultrasensitive, selective, and humidity-independent gas detection. ACS Appl Mater Interfaces. 2018;10(33):27858-27867. https://doi.org/10.1021/acsami.8b09169
3. Shaik R, Kampara RK, Kumar A, Sharma CS, Kumar M. Metal oxide nanofibers based chemiresistive H_2S gas sensors. Coord Chem Rev. 2022;471:214752. https://doi.org/10.1016/j.ccr.2022.214752

https://doi.org/10.61577/jnd.2026.100007

4. Nikolic MV, Milovanovic V, Vasiljevic ZZ, Stamenkovic Z. Semiconductor gas sensors: Materials, technology, design, and application. Sensors (Basel, Switzerland). 2020;20(22):6694. https://doi.org/10.3390/s20226694
5. Zhang R, Qin C, Bala H, Wang Y, Cao J. Recent progress in spinel ferrite (MFe_2O_4) chemiresistive based gas sensors. Nanomaterials. 2023;13(15):2188. https://doi.org/10.3390/nano13152188
6. Mataev M, Madiyarova A, Abdraimova M, Tursyn Z, Ramachandran K. Structure property–application relationships of spinel ferrite nanoparticles: From synthesis to functional systems. Int J Mol Sci. 2026;27(5):2096. https://doi.org/10.3390/ijms27052096
7. Wu K, Li J, Zhang C. Zinc ferrite based gas sensors: A review. Ceram Int. 2019;45(9):11143-11157. https://doi.org/10.1016/j.ceramint.2019.03.086
8. Xuan J, Zhao G, Sun M, Jia F, Wang X, Zhou T, et al. Low-temperature operating ZnO-based NO_2 sensors: A review. RSC advances. 2020;10(65):39786-39807. https://doi.org/10.1039/d0ra07328h
9. Sanchez-Lievanos KR, Stair JL, Knowles KE. Cation distribution in spinel ferrite nanocrystals: Characterization, impact on their physical properties, and opportunities for synthetic control. Inorg Chem. 2021;60(7):4291-4305. https://doi.org/10.1021/acs.inorgchem.1c00040
10. Andersen HL, Saura-Múzquiz M, Granados-Miralles C, Canévet E, Lock N, Christensen M. Crystalline and magnetic structure–property relationship in spinel ferrite nanoparticles. Nanoscale. 2018;10(31):14902-14914. https://doi.org/10.1039/c8nr01534a
11. Li J, Cheepurupalli KK, English NJ, Bandaru S, Zhang X. Unraveling cation distribution and defect roles in substituted ferrite performance: An atomistic DFT study. J Appl Phys. 2025;138(12). https://doi.org/10.1063/5.0287154
12. Javed M, Khan AA, Kazmi J, Mohamed MA, Khan MN, Hussain M, et al. Dielectric relaxation and small polaron hopping transport in sol-gel-derived $NiCr_2O_4$ spinel chromite. Mater Res Bull. 2021;138:111242. https://doi.org/10.1016/j.materresbull.2021.111242
13. Iqbal Y, Shah WH, Khan B, Javed M, Ullah H, Khan N, et al. Small polaron hopping transport mechanism, dielectric relaxation and electrical conduction in $NiAl_2O_4$ electro-ceramic spinel oxide. Phys Scr. 2023;98(6):065951. https://doi.org/10.1088/1402-4896/acd5ba
14. Nath VG, Ray S, Rodney JD, Bharath SP, Roy S, Tarafder K, et al. Mechanistic insight and first principle analysis of cation-inverted zinc ferrite nanostructure: A paradigm for ppb-level room temperature NOx sensor. Chem Eng J. 2024;490:151873. https://doi.org/10.1016/j.cej.2024.151873
15. Tatarchuk T. Studying the defects in spinel compounds: discovery, formation mechanisms, classification, and influence on catalytic properties. Nanomaterials. 2024;14(20):1640. https://doi.org/10.3390/nano14201640
16. Yang S, Lei G, Xu H, Lan Z, Wang Z, Gu H. Metal oxide based heterojunctions for gas sensors: A review. Nanomaterials. 2021;11(4):1026. https://doi.org/10.3390/nano11041026
17. Kotresh S, Ravikiran YT, Vijayakumari SC, Thomas S. Interfacial pn heterojunction of polyaniline-nickel ferrite nanocomposite as room temperature liquefied petroleum gas sensor. Composite Interfaces. 2017;24(6):549-561. https://doi.org/10.1080/09276440.2017.1241523
18. Liang J, Zou Z, Zhao Z, Hui B, Tian W, Zhang K. Intelligent gas detection: g-C_3N_4/polypyrrole decorated alginate paper as smart selective NH_3/NO_2 sensors at room temperature. Inorganic Chemistry. 2024;63(27):12516-12524. https://doi.org/10.1021/acs.inorgchem.4c01242
19. Huo Y, Qiu L, Wang T, Yu H, Yang W, Dong X, et al. P–n Heterojunction formation: metal sulfide@ metal oxide chemiresistor for Ppb H_2S detection from exhaled breath and food spoilage at flexible room temperature. ACS sensors. 2024;9(6):3433-3443. https://doi.org/10.1021/acssensors.4c00866
20. Mkwae PS, Kortidis I, Kroon RE, Leshabane N, Jozela M, Swart HC, et al. Insightful acetone gas sensing behaviour of Ce substituted $MgFe_2O_4$ spinel nano-ferrites. J Mater Res Technol. 2020;9(6):16252-16269. https://doi.org/10.1016/j.jmrt.2020.11.079
21. Norizan MN, Abdullah N, Halim NA, Demon SZ, Mohamad IS. Heterojunctions of rGO/metal oxide nanocomposites as promising gas-sensing materials—A review. Nanomaterials. 2022;12(13):2278. https://doi.org/10.3390/nano12132278
22. Yan Y, Yang G, Xu JL, Zhang M, Kuo CC, Wang SD. Conducting polymer-inorganic nanocomposite-based gas sensors: A review. Sci Technol Adv Mater. 2020;21(1):768-786. https://doi.org/10.1080/14686996.2020.1820845
23. Alharthy RD, Saleh A. A novel trace-level ammonia gas sensing based on flexible PAni-$CoFe_2O_4$ nanocomposite film at room temperature. Polymers. 2021;13(18):3077. https://doi.org/10.3390/polym13183077
24. Ramasamy T, Satheesh LG, Selvaraj V, Bazaka O, Levchenko I, Bazaka K, et al. Spinel $CoFe_2O_4$ nanoflakes: A path to enhance energy generation and environmental remediation potential of waste-derived rGO. Nanomaterials. 2022;12(21):3822. https://doi.org/10.3390/nano12213822
25. Dojcinovic MP, Vasiljevic ZZ, Pavlovic VP, Barisic D, Pajic D, Tadic NB, et al. Mixed Mg–Co spinel ferrites: Structure, morphology, magnetic and photocatalytic properties. J Alloys Compd. 2021;855:157429. https://doi.org/10.1016/j.jallcom.2020.157429
26. Soudani I, Ben Brahim K, Oueslati A, Slimi H, Aydi A, Khirouni K. Investigation of structural, morphological, and transport properties of a multifunctional Li-ferrite compound. RSC Advances. 2022;12(29):18697-18708. https://doi.org/10.1039/d2ra02757g
27. Chen H, Chen H, Chen J, Song M. Gas sensors based on semiconductor metal oxides fabricated by electrospinning: A review. Sensors. 2024;24(10):2962. https://doi.org/10.3390/s24102962
28. Pham TN, Dinh NX, Lan NT, Van Quy N, Bach TN, Lam VD, et al. Toward a comprehensive understanding of effect of cation distribution and M2+ constituent in spinel ferrite nanocrystals MFe_2O_4 (M= Co, Mn, and Ni) on the electrochemical response in sensitive detection of chloramphenicol. J Alloys Compd. 2023;949:169880. https://doi.org/10.1016/j.jallcom.2023.169880
29. Bhargava A, Eppstein R, Sun J, Smeaton MA, Paik H, Kourkoutis LF, et al. Breakdown of the small-polaron hopping model in higher-order spinels. Adv Mater. 2020;32(49):2004490. https://doi.org/10.1002/adma.202004490
30. Sopiha KV, Malyi OI, Persson C, Wu P. Chemistry of oxygen ionosorption on SnO_2 surfaces. ACS Appl Mater Interfaces. 2021;13(28):33664. https://doi.org/10.1021/acsami.1c08236
31. Njoroge MA, Kirimi NM, Kuria KP. Spinel ferrites gas sensors: a review of sensing parameters, mechanism and the effects of ion substitution. Crit Rev Solid State Mater. Sci. 2022;47(6):807-836. https://doi.org/10.1080/10408436.2021.1935213
32. Mirabella DA, Aldao CM. Dependence of n-Type metal-oxide gas sensor response on the pressure of oxygen and reducing gases. ACS Sensors. 2024;9(4):1938-1944. https://doi.org/10.1021/acssensors.3c02674
33. Ciftyurek E, Li Z, Schierbaum K. Adsorbed oxygen ions and oxygen vacancies: Their concentration and distribution in metal oxide chemical sensors and influencing role in sensitivity and sensing mechanisms. Sensors. 2022;23(1):29. https://doi.org/10.3390/s23010029
34. Jung G, Ju S, Choi K, Kim J, Hong S, Park J, et al. Reconfigurable manipulation of oxygen content on metal oxide surfaces and applications to gas sensing. ACS Nano. 2023;17(18):17790-17798. https://doi.org/10.1021/acsnano.3c03034
35. Leve ZD, Iwuoha EI, Ross N. The synergistic properties and gas sensing performance of functionalized graphene-based sensors. Materials. 2022;15(4):1326. https://doi.org/10.3390/ma15041326
36. Ahmad SI. A review on synthesis and magnetic hyperthermia application of spinel nano ferrite. J Umm Al-Qura Univ Appl Sci. 2025:1-45. https://doi.org/10.1007/s43994-025-00262-1
37. Sagayaraj R, Aravazhi S, Chandrasekaran GJ. Review on structural and magnetic properties of (Co–Zn) ferrite nanoparticles. Int Nano Lett. 2021;11(4):307-319. https://doi.org/10.1007/s40089-021-00343-z
38. Duarte FS, Melo A, Oliveira L, Duarte J, Oliveira R. Green synthesis for antibiotic photodegradation: Recent advances and future trends. Water. 2025;18(1):39. https://doi.org/10.3390/w18010039
39. Krishna KG, Parne S, Pothukanuri N, Kathirvelu V, Gandi S, Joshi D. Nanostructured metal oxide semiconductor-based gas sensors: A comprehensive review. Sens Actuators A: Phys. 2022;341:113578. https://doi.org/10.1016/j.sna.2022.113578
40. Uma S, Shobana MK. Band structure and mechanism of semiconductor metal oxide heterojunction gas

https://doi.org/10.61577/jnd.2026.100007

sensor. Inorg Chem Commun. 2024;160:111941. https://doi.org/10.1016/j.inoche.2023.111941

41. Powar RR, Parale VG, Phadtare VD, Wategaonkar SB, Mane RK, Gunjkar JL, et al. Nanocrystalline spinel zinc-substituted cobalt ferrite thick film an efficient ethanol sensor. Mater Today Chem. 2021;22:100607. https://doi.org/10.1016/j.mtchem.2021.100607
42. Nasri A, Petrissans M, Fierro V, Celzard A. Gas sensing based on organic composite materials: Review of sensor types, progresses and challenges. Mater Sci Semicond Process. 2021;128:105744. https://doi.org/10.1016/j.mssp.2021.105744
43. Imash A, Smagulova G, Kaidar B, Keneshbekova A, Kazhdanbekov R, Velasco LF, et al. Chemoresistive gas sensors based on electrospun 1D nanostructures: Synergizing morphology and performance optimization. Sensors. 2024;24(21):6797. https://doi.org/10.3390/s24216797
44. Gai LY, Lai RP, Dong XH, Wu X, Luan QT, Wang J, et al. Recent advances in ethanol gas sensors based on metal oxide semiconductor heterojunctions. Rare Met. 2022;41(6):1818-1842. https://doi.org/10.1007/s12598-021-01937-4
45. Mugutkar AB, Gore SK, Patange SM, Mane RS, Raut SD, Shaikh SF, et al. Ammonia gas sensing and magnetic permeability of enhanced surface area and high porosity lanthanum substituted Co–Zn nano ferrites. Ceram Int. 2022;48(11):15043-15055. https://doi.org/10.1016/j.ceramint.2022.02.033
46. Vishnuraj R, Karuppanan KK, Aleem M, Pullithadathil B. Boosting the performance of NO_2 gas sensors based on n–n type mesoporous ZnO@ In_2O_3 heterojunction nanowires: *In situ* conducting probe atomic force microscopic elucidation of room temperature local electron transport. Nanoscale Adv. 2020;2(10):4785-4797. https://doi.org/10.1039/d0na00318b
47. Mu Y, Ma ZH, Liang HS, Zhang LM, Wu HJ. Ferrite-based composites and morphology-controlled absorbers. Rare Metals. 2022;41(9):2943-2970. https://doi.org/10.1007/s12598-022-02045-7
48. Jian Y, Hu W, Zhao Z, Cheng P, Haick H, Yao M, et al. Gas sensors based on chemi-resistive hybrid functional nanomaterials. Nano-Micro Lett. 2020;12(1):71. https://doi.org/10.1007/s40820-020-0407-5
49. Chen Y, Cao Y. Ultrasensitive and low detection limit of acetone gas sensor based on ZnO/SnO_2 thick films. RSC Adv. 2020;10(59):35958-35965. https://doi.org/10.1039/d0ra06406h
50. Sun K, Zhan G, Chen H, Lin S. Low-operating-temperature NO_2 sensor based on a CeO_2/ZnO heterojunction. Sensors. 2021;21(24):8269. https://doi.org/10.3390/s21248269

https://doi.org/10.61577/jnd.2026.100007